# Support Information

## Polymeric Artificial Solid Electrolyte Interface Dramatically Enhances Lithium-Ions Transport

Chun Li, Bin Hu, Yujuan Wang, Kedong Bi*

Jiangsu Key Laboratory for Design and Manufacture of Micro-Nano Biomedical Instruments, School of Mechanical Engineering, Southeast University, Nanjing 211189, P. R. China

## Model

The initial configurations of lithium hexafluorophosphate ($LiPF_6$) and ethylene carbonate (EC) molecules were modeled using Materials Studio, and their atomic coordinates were optimized via PACKMOL for molecular dynamics simulations[1]. The anode consists of an eight-layered stacked graphite structure with an armchair edge. Dangling carbon atoms on one edge were randomly functionalized with hydroxyl and carboxyl groups, while the other edge's dangling carbon atoms were fully hydrogenated to avoid the effects of unsaturation. The artificial solid electrolyte interface (A-SEI) structure was constructed using Polythiophene (PTh) chains placed in a $45 \times 51 \times 22$ Å$^3$ box using the Amorphous Cell Module of Materials Studio. Subsequently, the nanobattery model (Figure 1), including the graphitic anode, the PTh (A-SEI) layer, and the electrolyte solution, was created in a simulation box measuring $45 \times 51 \times 175$ Å$^3$. Additionally, two graphene layers were placed at the end edge of the simulation box near the electrolyte to prevent unreasonable movement of electrolyte molecules.

## Force Fields

$LiPF_6$ dissolved into $Li^+$ cations and $PF_6^-$ anions in EC yield the electrolyte solution. The intramolecular interactions are model by the CFF93 force field[2], besides, specific bonds, angles, dihedrals, and improper dihedrals parameters for $LiPF_6$ and EC are acquired from quantum chemical calculations[3] (Table S1).

**Table S1.** Geometry Optimized Parameters for Ethylene Carbonate Obtained with the B3PW91/cc-pVTZ Level of Theory

| Atom1 | Atom2 | Atom3 | Atom4 | Bond 1-2 (Å) | Angle 1-2-3 (deg) | Dihedral 1-2-3-4 (deg) |
|---|---|---|---|---|---|---|
| Ox | Cs | Os | Os/Ch | 1.186 | 124.8 | 180.0/-172.8 |
| Os | Cs | Os | Ch | 1.354 | 110.3 | 7.2 |
| Os | Ch | Ch | Os | 1.426 | 103.0 | 20.3 |
| Os | Ch | Ch | H | 1.426 | 103.0 | 117.2/-96.9/138.0 |
| Ch | Ch | H | H | 1.525 | 112.7 | 126.9 |
| Cs | Os | Ch | Ch | 1.354 | 109.6 | -17.2 |
| Cs | Os | Ch | H | 1.354 | 109.6 | 102.6/-138.1 |
| Os | Ch | H | H | 1.426 | 108.9 | 119.0 |
| H | Ch | Ch | H | 1.090 | 112.7 | 20.8/-104.4/146.0 |
| H | Ch | H | | 1.090 | 109.5 | |

The intermolecular interactions are taken from the Lennard-Jones (12-6 LJ) pair interaction model and the force field parameters between the atoms of EC, $Li^+$, $PF_6^-$ PTh, and graphite using averaging rules for pairs of different type of atoms. The depth $\varepsilon$ and length $\sigma$ parameters are listed in Table S2. Other pairs of atoms not shown in Table S2 was estimated using the Combination rules, $\sigma_{12} = (\sigma_1 + \sigma_2)/2$ and $\varepsilon_{12} = \sqrt{\varepsilon_1 \varepsilon_2}$. Moreover, the CVFF force field to recognize to be reliable for the interatomic potential of PTh and the interaction among PTh, graphite, and organic molecule because it is accurate in regard to the structure and binding energy of the model. The potential function is composed of bonded interactions and nonbonded interactions. The bonded

terms include bond stretch, bond angle bending, and dihedral angle torsion terms, while the nonbonded terms are composed of electrostatic and van der Waals interaction. The potential function *V(r)* in CVFF defining interactions among various atoms of the PTh is shown as

$$V(r) = \sum_b K_b(b-b_0)^2 + \sum_\theta K_\theta(\theta-\theta_0)^2 + \sum_\varphi K_\varphi(1+\mathrm{d}\cos n\varphi_0) + \sum_{i,j} 4\varepsilon_{ij}\left[\left(\frac{\sigma_{ij}}{r_{ij}}\right)^{12} - \left(\frac{\sigma_{ij}}{r_{ij}}\right)^{6}\right] + \sum_{i,j}\frac{q_i q_j}{\varepsilon r_{ij}} \quad \text{(S1)}$$

where $b_0$, $\theta_0$, and $\varphi_0$ are equilibrium bond length, bond angle, and dihedral angle, respectively. $K_b$, $K_\theta$, and $K_\varphi$ are the corresponding energy coefficient, and $b$ and $\theta$ are the true bond length and bond angle. $r_{ij}$ is the distance between two atoms with charge $q_i$ and $q_j$.

The anode is composed of a crystal of graphite with functional groups on one side edge. To precisely model the interaction among the carbon atoms in the same layer of graphite and the interlayer interactions, the CVFF force field was adopted on the graphitic anode. In addition, the interaction between graphite anode and the solvent solution as well as all other nonbonded interactions are calculated with Lennard-Jones (12-6 LJ) potentials. Then, the optimized depth $\varepsilon$ and length $\sigma$ parameters are listed in Table S2.

**Table S2.** Modified and Original UFF Lennard-Jones Pair Potential Parameters

| Pair | ε/(kcal/mol) (modified) | σ/(Å) (modified) | ε/(kcal/mol) (UFF) | σ/(Å) (UFF) |
|---|---|---|---|---|
| Ox-Cgraphene | 0.1873 | 3.442 | 0.08 | 3.68 |
| Cx-Cgraphene | 0.2478 | 3.618 | 0.105 | 3.851 |
| Os-Cgraphene | 0.1873 | 3.442 | 0.08 | 3.68 |
| Ch-Cgraphene | 0.2478 | 3.618 | 0.105 | 3.851 |
| H-Cgraphene | 0.1604 | 3.135 | 0.068 | 3.37 |
| Li-Li | 0.305 | 2.051 | 0.025 | 2.451 |
| Li-O | 0.6 | 1.4 | 0.039 | 2.98 |
| C(EC,graphene) | 0.105 | 3.851 | 0.105 | 3.851 |

| | | | | |
|---|---|---|---|---|
| F($LiPF_6$)-graphene | 0.171 | 3.374 | 0.072 | 3.60 |
| Li($LiPF_6$)-graphene | 0.051 | 2.00 | 0.051 | 3.15 |
| H(EC) | | | 0.044 | 2.886 |
| P($LiPF_6$) | | | 0.305 | 4.147 |
| F($LiPF_6$) | | | 0.05 | 3.364 |
| Li($LiPF_6$) | | | 0.025 | 2.451 |

The charge of atoms is acquired by Mulliken and natural bond orbital (NBO) populations for calculation of Coulomb interactions[4] (Table S3). The potential obtained using Mulliken populations is valid, which they match accurately with the one calculated by NBO charges[3]. In addition, the influence of fluorine atoms needs to be considered in this system. Fluorine atoms could generate σ-holes which is a non-covalent interaction between a negative site and a covalently bonded fluorine[5-7]. Fortunately, owing to the huge difference of electronegativity in F and P atoms (4 and 2.1, respectively), the proportion of covalent bonding in $PF_6^-$ is merely 0.4. Hence, the effective σ-holes caused by fluorine atoms are ignorable despite the vicinity each fluorine atom of the $PF_6^-$ ion have been confirmed to include the lowest negative potential[8].

**Table S3.** Mulliken Populations Obtained with the B3PW91/cc-pVTZ Level of Theory

| Atom | Q/e |
|---|---|
| Ox(EC) | -0.46 |
| Cx(EC) | 0.81 |
| Os(EC) | -0.45 |
| Ch(EC) | -0.12 |
| H(EC) | 0.20 |
| Li($LiPF_6$) | 1.00 |
| P($LiPF_6$) | 1.34 |

| | |
|---|---|
| $F(LiPF_6)$ | -0.39 |

**Simulation details**

Classical MD simulations are conducted to investigate the effect of the PTh acting as A-SEI layer and Li-ion migration kinetics of the A-SEI using the large-scale atomic/molecular massively parallel simulator (LAMMPS) program and Materials Studio. Firstly, the configuration optimization of the initially built model is performed to obtain the reasonable geometry. After geometry optimization, a temperature equilibration at 20 K for 2 ns using the NVT ensemble[9] to remove hot spots in the model. Then, the temperature is increased from 20 to 320 K in 6 ns with an interval of 50 K and is equilibrated at 320 K for 2 ns under the NVT ensemble. Afterward, for observing the migration path of Li+, the electric field is applied along the z-axis direction (horizontal direction) of the nonobattery model with an intensity equaling $0.5\ V/Å$ under the NPT ensemble. The Nosé-Hoover thermostat[10, 11] and barostat[12] are applied to maintain the temperature and pressure at the MD simulations. The periodic boundary condition was applied to x and y directions, and the reflecting boundary condition was implemented along the z-direction. The reflecting walls reflect atoms back to the simulation cell if they attempt to move outside the wall. During charging, $Li^+$ travel from the electrolyte to the graphite anode because of the action of the external electric field. The visualization of trajectories is accomplished via an open-source tool: Visualization Molecular Dynamics (VMD)[13]

The designed Li-ion battery model, with PTh serving as the artificial solid-electrolyte interface, was equilibrated at 50 K for 2 ns. During this period, the system's energy minimized from -22874 kJ/mol to -22901 kJ/mol. Subsequently, the cell was heated from 50 K to 300 K at a rate of 83 mK/ps. This heating process caused the total energy (E) to increase from -22901 kJ/mol to -19439 kJ/mol (Figure S1). After heating, the battery was equilibrated for 7 ns at 300 K under the NVT ensemble. The models, depicted in the inset of Figure S1, illustrate the intermediate state during the configuration optimization process. Upon reaching thermodynamic equilibrium, the total energy of the cell stabilized at -19350 kJ/mol with negligible fluctuations.

Therefore, the nanobattery is suitable for further thermodynamic simulations to investigate its performance and structural characteristics, as no significant changes in total energy were observed.

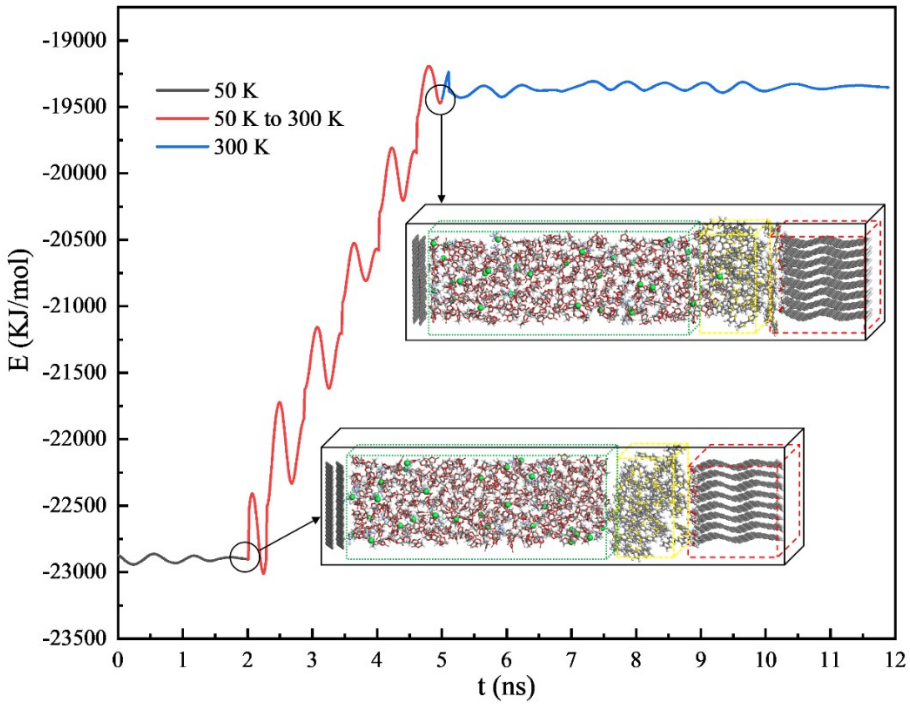


**Figure S1.** Total energy evolution during the equilibration and heating process.

## Verification the Model

The radial distribution functions (RDFs) of $Li^+$ ions and the carbonyl oxygen ($O_c$) in EC molecules were calculated at various temperatures (Figure S2). For EC, the RDFs exhibit decreased structural order with rising temperature, although the peak positions remain largely unchanged. This structural robustness suggests that the electrolyte maintains relative stability under thermal variation. Our simulation results are consistent with previous data[14], indicating that the model we designed is reasonable.

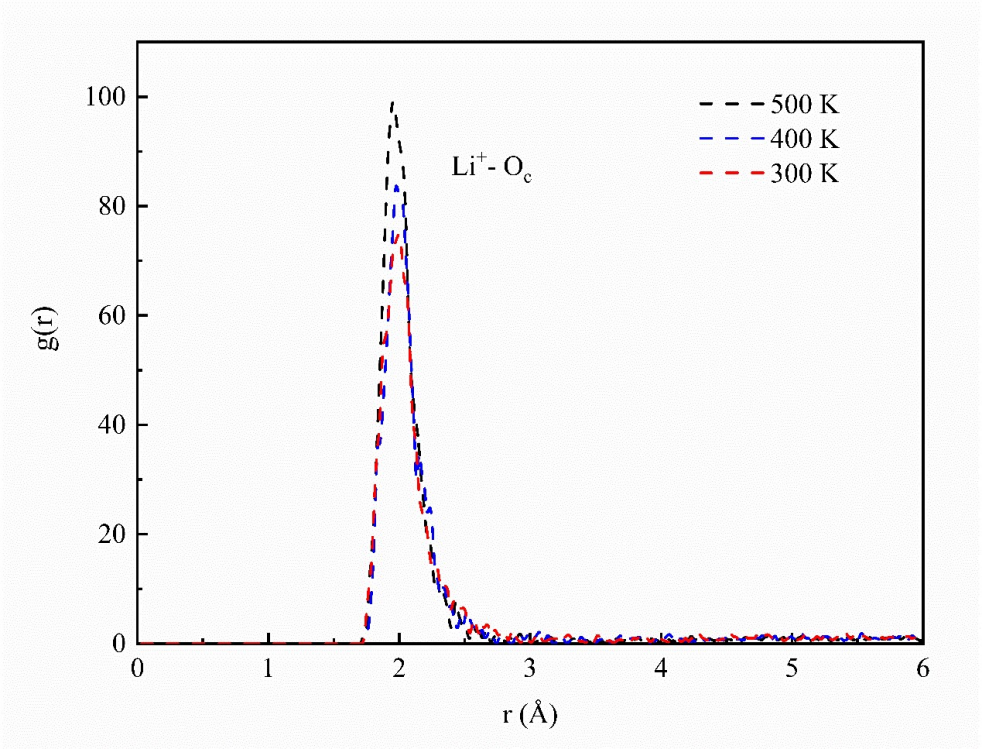


**Figure S2.** Radial distribution functions, g(*r*), for $Li^+$-$O_c$ at various temperatures.

## Charge Process of the Battery

The external electric field *E* is applied to study the charging of the battery after the thermodynamic equilibration process. Due to the influence of an applied external electric field, Li-ions migrate from the electrolyte solution to the negative electrode, while $PF6^-$ ions drift in the opposite direction. The Li-ions are solvated by EC molecules, and their motion induces translational movement in the surrounding EC molecules. The external electric field causes only slight rotational motion of the EC molecules because the interaction between the dipole moments of EC and the electric field is extremely weak.

As shown in Figure S3b, prior to the application of the electric field, no Li-ions are present in the graphite anode. However, after 10 ps of electric field application, 30 Li-ions are stored within the graphite layers. Initially, PF6-ions are evenly distributed throughout the electrolyte solution due to the complete dissolution of lithium hexafluorophosphate ($LiPF_6$) in the EC solution. Upon applying the electric field, $PF_6$-ions migrate to the side opposite the graphite anode, leading to slight polarization of the electrolyte solution.

By the 10th ps, all Li-ions are stored in the graphite layers, marking the end of the battery charging process. As lithium ions gradually intercalate into the graphite layers, the interlayer spacing increases, causing the graphite structure to become wavy. Once the Li+ ions reach the anode and are reduced within the graphite layers, they tend to occupy bridge and hole sites and remain stationary. Throughout the charging process, the number of Li-ions reaching the graphite anode increases steadily, resulting in a stable ionic current.

To ensure sufficient lithium ion migration through the PTh embedded in the anode layers within computationally practical times, simulations were performed for up to 40 ps at an electric field strength of 0.5 V/Å, ensuring an adequate number of ions reached the anode.

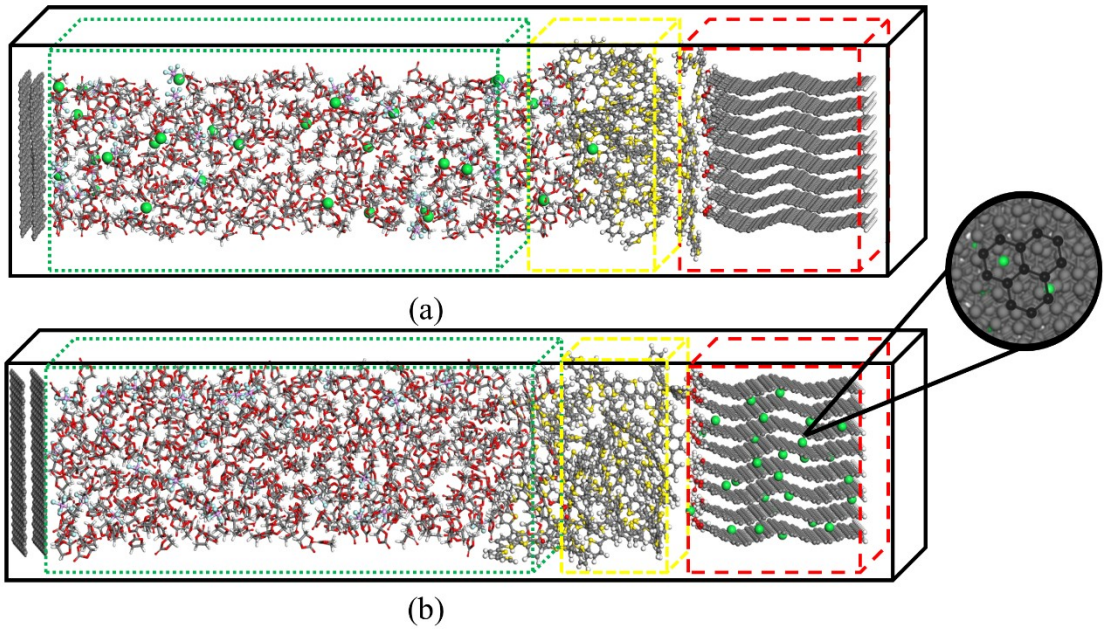


**Figure S3.** Snapshots taken during the charge of the model. (a) The model after thermodynamic equilibrium without external electric field. (b) Snapshot of an overcharged model at 10 ps, showing the Li-atom interstitial and centered in a carbon ring.

## The self-part of the van Hove function for $Li^+$ transport

The transport mechanism of $Li^+$ through the PTh matrix is further investigated by the van Hove time correlation function which demonstrates the distribution of $Li^+$ displacement with time. Consider a set of $N$ where The van Hove function $G(\mathbf{r},t)$ defined as

$$G(\mathbf{r},t)=\frac{1}{N}\left\langle \sum_{i=1}^{N}\sum_{j=1}^{N}\delta\left(\mathbf{r}-\mathbf{r}_i(t)+\mathbf{r}_j(0)\right)\right\rangle \tag{S2}$$

where $i=1,..,N$ is the particle index. $\mathbf{r}_i(t)$ represents the position coordinate of particle $i$ at time t. $\langle\cdot\rangle$ and $\delta(\cdot)$ are the ensemble average and the three-dimensional Dirac delta function, respectively.

The van Hove function for Li-ion is the probability density of finding a Li-ion by $r$ from its initial position at time $t$. $G(\mathbf{r},t)$can be naturally decomposed into two terms,

conventionally referred to as its "self" and "distinct" part, by discriminating between the cases $i = j$ and $i \neq j$, respectively.

$$G(\mathbf{r},t)=\frac{1}{N}\left\langle\sum_{i=1}^{N}\delta\left(\mathbf{r}+\mathbf{r}_i(0)-\mathbf{r}_i(t)\right)\right\rangle+\frac{1}{N}\left\langle\sum_{i\neq j}^{N}\delta\left(\mathbf{r}+\mathbf{r}_j(0)-\mathbf{r}_j(t)\right)\right\rangle=G_{\mathrm{s}}(\mathbf{r},t)+G_{\mathrm{d}}(\mathbf{r},t) \tag{S3}$$

$$G(\mathbf{r},t)=G_{\mathrm{s}}(\mathbf{r},t)+G_{\mathrm{d}}(\mathbf{r},t) \tag{S4}$$

The volume integral of $G_s(\mathbf{r},t)$ is a constant at any time, that is

$$\int_0^{\infty}4\pi \mathrm{r}^2 G_s(\mathbf{r},t)\mathrm{d}r=1 \tag{S5}$$

where the $4\pi r^2 G_s(\mathbf{r},t)$ is the probability that a $Li^+$ has moved a distance $r$ within the time $t$.

As shown in Figure S4, at the time t = 3 ps, the function $4\pi r^2 G_s(\mathbf{r},t)$ of the nanobattery decay rapidly to zero at a very short distance. This is because the lithium ions surrounded by EC molecules move in the electrolyte at the beginning and have not been desolvated into the PTh matrix. However, at the time t = 30 ps, the appearance of a secondary peak in the $4\pi r^2 G_s(\mathbf{r},t)$ curve at r = 22 Å verifies that the $Li^+$ hopping phenomenon occurs when Li-ions pass through the PTh matrix, as depicted in Figure S4, suggesting that the PTh chains provide a transport path for $Li^+$ migration.

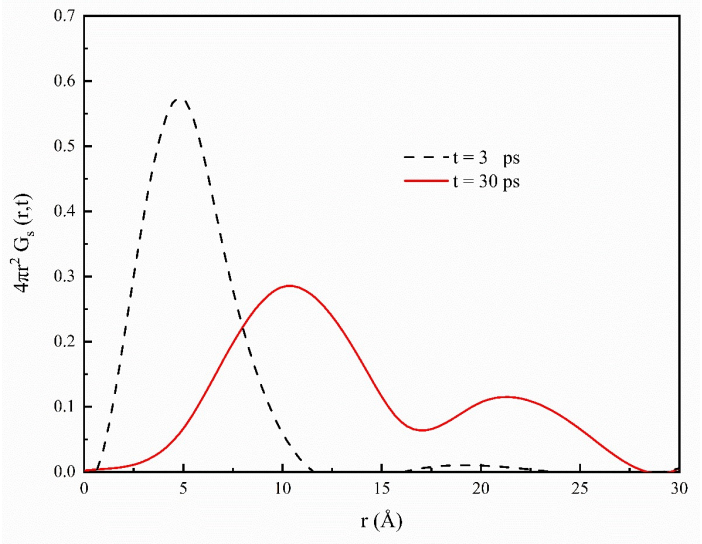


**Figure S4.** Self-part of the van Hove correlation functions $4\pi r^2 G_s(\mathbf{r},t)$ of $Li^+$ at time t = 3 ps and t = 30 ps in the PTh matrix.

## Conductivity aligning with the VFT model

Ionic conductivity ($\sigma_{ic}$) quantifies the ability of the $Li^+$ motion in the battery. Molar conductivity ($\wedge$) can be obtained via Einstein's relation,

$$\wedge=\frac{N_A e^2}{6nk_B T}\lim_{t\to\infty}\frac{d}{dt}\sum_i\sum_j z_i z_j\left\langle \Delta r_i\cdot\Delta r_j\right\rangle \quad \text{(S6)}$$

$$\sigma_{ic}=c\wedge \quad \text{(S7)}$$

where $N_A$ is Avogadro's number, $e$ is an electron charge, $n$ is the total number of ions ($Li^+$ and $PF_6^-$), $k_B$ is Boltzmann constant, and $z_i$ is the charge on ion $i$. $\Delta r_i = r_i(t) - r_i(0)$ is the displacement of ion $i$. $c$ is the concentration of the electrolyte solution, $\sigma_{ic}$ is the ionic conductivity.

As Figure S5 shown, the ionic conductivity increases with an increased temperature, and the logarithms of the ionic conductivity show approximately linear relation with 1/T by fitting the ionic conductivity data. It can be described by the VTF equation:

$$\sigma=\sigma_0 T^{-\frac{1}{2}}\exp\left(-\frac{B}{T-T_0}\right) \quad \text{(S8)}$$

where $\sigma_0$ is fitting constants, $B$ is the pseudo-activation energy for the conductivity, and $T_0$ is the reference temperature which is related to $T_g$.

The VFT model describes the temperature-dependent, nonlinear conductive behavior of lithium ions in disordered or glassy materials. When the conductivity aligns with the VFT model, it suggests that the lithium ion migration process involves overcoming local energy barriers, akin to a hopping mechanism. Additionally, the nonlinear temperature dependence indicates that at lower temperatures, lithium ion hopping is hindered, resulting in a significant drop in conductivity. The phenomenon shown in Figure S5 aligns with the characteristic curve of the VFT model, indicating that the transport mechanism of lithium ions in PTh materials is achieved through a hopping process.

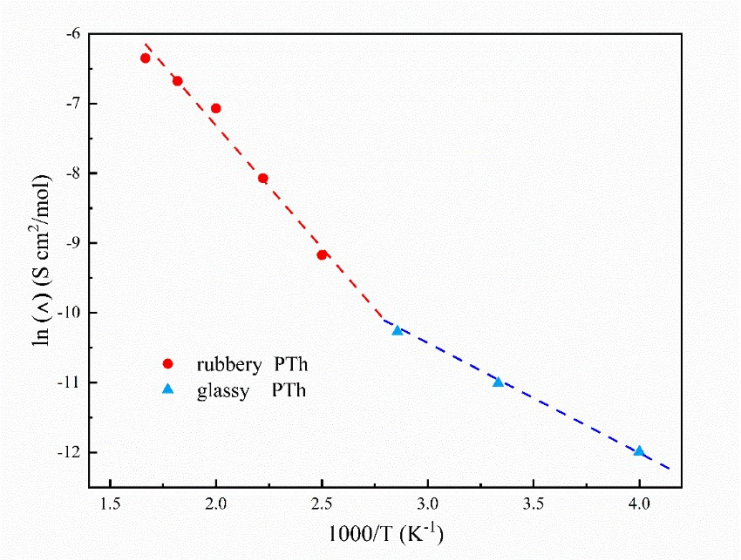


**Figure S5.** Effect of temperature on molar conductivity of the nanobattery model.

**Reference**


1. Martínez, L.; Andrade, R.; Birgin, E. G.; Martínez, J. M., PACKMOL: A package for building initial configurations for molecular dynamics simulations. *Journal of Computational Chemistry* **2009,** *30* (13), 2157-2164.
2. Sun, H.; Mumby, S. J.; Maple, J. R.; Hagler, A. T., An ab Initio CFF93 All-Atom Force Field for Polycarbonates. *Journal of the American Chemical Society* **1994,** *116* (7), 2978-2987.
3. Ponce, V.; Galvez-Aranda, D. E.; Seminario, J. M., Analysis of a Li-Ion Nanobattery with Graphite Anode Using Molecular Dynamics Simulations. *The Journal of Physical Chemistry C* **2017,** *121* (23), 12959-12971.
4. Kumar, N.; Seminario, J. M., Lithium-Ion Model Behavior in an Ethylene Carbonate Electrolyte Using Molecular Dynamics. *The Journal of Physical Chemistry C* **2016,** *120* (30), 16322-16332.
5. Politzer, P.; Murray, J. S.; Clark, T., Halogen bonding and other σ-hole interactions: a perspective. *Physical Chemistry Chemical Physics* **2013,** *15* (27), 11178-11189.
6. Murray, J. S.; Lane, P.; Politzer, P., Expansion of the σ-hole concept. *Journal of Molecular Modeling* **2009,** *15* (6), 723-729.
7. Murray, J. S.; Lane, P.; Clark, T.; Politzer, P., σ-hole bonding: molecules containing group VI atoms. *Journal of Molecular Modeling* **2007,** *13* (10), 1033-1038.
8. Cavallo, G.; Murray, J. S.; Politzer, P.; Pilati, T.; Ursini, M.; Resnati, G., Halogen bonding in hypervalent iodine and bromine derivatives: halonium salts. *IUCrJ* **2017,** *4* (4), 411-419.
9. Nauchitel, V. V., Energy distribution function for the NVT canonical ensemble. *Molecular Physics* **1981,** *42* (5), 1259-1265.
10. Nosé, S., A molecular dynamics method for simulations in the canonical ensemble. *Molecular Physics* **1984,** *52* (2), 255-268.
11. Hoover, W. G., Canonical dynamics: Equilibrium phase-space distributions. *Physical Review A* **1985,** *31* (3), 1695-1697.
12. Kalibaeva, G.; Ferrario, M.; Ciccotti, G., Constant pressure-constant temperature molecular dynamics: a correct constrained NPT ensemble using the molecular virial. *Molecular Physics* **2003,** *101* (6), 765-778.
13. Humphrey, W.; Dalke, A.; Schulten, K., VMD: Visual molecular dynamics. *J Mol Graph* **1996,** *14* (1), 33-38.
14. Muralidharan, A.; Chaudhari, M. I.; Pratt, L. R.; Rempe, S. B., Molecular Dynamics of Lithium Ion Transport in a Model Solid Electrolyte Interphase. *Sci Rep* **2018,** *8* (1), 10736.